Field-resolved spectroscopy approaching ultimate detection sensitivity

Ioachim Pupeza (ioachim.pupeza@mpq.mpg.de)
Max-Planck-Institut für Quantenoptik, Garching, Germany https://orcid.org/0000-0001-8422-667X
Christina Hofer
Max Planck Institute of Quantum Optics
Daniel Gerz
Ludwig Maximilians University Munich
Lukas Fürst
Ludwig Maximilians University Munich
Maximilian Högner
Max Planck Institute of Quantum Optics
Thomas Butler
Max Planck Institute of Quantum Optics
Martin Gebhardt
Institute of Applied Physics, Abbe Centre of Photonics, Friedrich Schiller University Jena
Tobias Heuermann
Institute of Applied Physics, Abbe Centre of Photonics, Friedrich Schiller University Jena
Christian Gaida
Active Fibre Systems GmbH, Jena, Germany
Kiran Maiti
Max Planck Institute of Quantum Optics
Marinus Huber
Ludwig Maximilians University Munich
Ernst Fill
Max-Planck-Institut für Quantenoptik
Jens Limpert
Institute of Applied Physics, Abbe Centre of Photonics, Friedrich Schiller University Jena
Ferenc Krausz
Max Planck Institute of Quantum Optics https://orcid.org/0000-0002-6525-9449

Physical Sciences - Article

Keywords:

Posted Date: May 13th, 2022

DOI: https://doi.org/10.21203/rs.3.rs-1622493/v1

Field-resolved spectroscopy approaching ultimate detection sensitivity

Authors:

Christina Hofer[1,2,3†], Daniel Gerz[1,2,4†], Lukas Fürst[1], Maximilian Högner[2], Thomas Patrick Butler[2], Martin Gebhardt[5,6,7], Tobias Heuermann[5,6,7], Christian Gaida[8], Kiran Sankar Maiti[2], Marinus Huber[1,2], Ernst Fill[2], Jens Limpert[5,6,7,8], Ferenc Krausz[1,2,3] and Ioachim Pupeza[1,2*]

Affiliations:

[1]Ludwig Maximilians University Munich, Garching, Germany

[2]Max Planck Institute of Quantum Optics, Garching, Germany

[3]Center for Molecular Fingerprinting, Molekuláris-Ujjlenyomat Kutató Közhasznú Nonprofit Kft., Budapest, Hungary

[4]Leibniz Institute of Photonic Technology - Member of the research alliance "Leibniz Health Technologies", Jena, Germany

[5]Institute of Applied Physics, Abbe Centre of Photonics, Friedrich Schiller University Jena, Germany

[6]Helmholtz-Institute Jena, Germany

[7]Gesellschaft für Schwerionenforschung, Darmstadt, Germany

[8]Active Fibre Systems GmbH, Jena, Germany

†These authors contributed equally to this work

*Corresponding author. Email: ioachim.pupeza@mpq.mpg.de

Electric-field oscillations are now experimentally accessible in the THz-to-PHz frequency range[1–11]. Their measurement delivers the most comprehensive information content attainable by optical spectroscopy – if performed with high sensitivity. Yet, the trade-off between bandwidth and efficiency associated with the nonlinear mixing necessary for field sampling has so far strongly restricted sensitivity in applications such as field-resolved spectroscopy of molecular vibrations[12,13]. Here, we demonstrate electric-field sampling of octave-spanning mid-infrared waves in the 18-to-39 THz (600-to-1300 cm^{-1}) spectral region, with amplitudes ranging from the MV/cm level down to a few mV/cm. Employing powerful short-wave mid-infrared gate pulses[14,15], the field-measurement sensitivity approaches within a factor of 4 the ultimate detection limit of capturing all photons in the temporal gate. This combination of detection sensitivity and dynamic range enables optimum use of newly-emerging high-power waveform-controlled infrared sources[12,14,16–22] for molecular spectroscopy. In a proof-of concept experiment, we performed broadband quantitative linear spectroscopy of multiple gases over more than 8 orders of magnitude in concentration, at an interaction length of only 45 cm. Our technique brings fast, label-free, quantitative multivariate detection of volatile organic compounds over the entire known physiologically-relevant molecular landscape[23,24] within reach.

Among quantitative multivariate molecular analysis techniques, broadband vibrational spectroscopies[25] uniquely combine several advantages. They require minimal sample preparation, and the specific “vibrational fingerprint” signal is acquired via optical interrogation, non-destructively and in a label-free manner. Recent progress in broadband, coherent sources of ultrashort mid-infrared (MIR) pulses is heralding a vast new potential for sensitivity and specificity in vibrational spectroscopy, in particular for molecular gases. On one hand, the bright vibrational fingerprints generated by their Watt-level average powers[12,14,16–22] afford the potential of highly-multivariate detection in a matter of minutes (Supplementary Information section I). On the other hand, their temporal coherence enables time-domain electric-field sampling[26]. This has recently proven a power and bandwidth scalability[12,13] superior to traditional, time-integrating spectroscopies[27–30], thereby possibly providing a means of optimally detecting vibrational fingerprints.

First quantitative MIR vibrational spectroscopy experiments employing electro-optic sampling (EOS)[1–3] have achieved the most sensitive broadband infrared spectroscopy of biological systems to date[12], and dual-frequency-comb spectroscopy over the entire molecular fingerprint region[13,31]. However, while these represent breakthrough results, the photon detection efficiency has stayed well below 1% (Supplementary Information section II). Furthermore, the range of quantified molecular concentrations has remained below 6 orders of magnitude, for both field-resolved and state-of-the-art time-integrating broadband vibrational spectroscopies[13,32,33] (see also Extended Data Table 1).

Here, we demonstrate electric-field sampling with photon detection efficiencies of up to 17%, and an average of 7.5% throughout the 600-to-1300-cm^{-1} spectral region. This exceeds the previous sensitivity record in the MIR range[12], (Extended Data Table 2) by more than one order of magnitude while simultaneously doubling the detection bandwidth. Because the electric-field strength scales with the square root of the number of photons, this implies a field measurement sensitivity close to the ultimate limit of detecting all photons in the interaction time window of the gate pulse with the MIR wave. In a benchmark experiment, we recorded the coherent response of multiple gases contained in a 45-cm-long cell to resonant excitation with broadband, waveform-stable MIR pulses. The linearity of the measured signals for concentrations spanning more than 8 orders of magnitude, from the sub-ppb range to vapor pressure, is confirmed.

High-sensitivity optical-field sampling

Drawing on preliminary experiments[14,34], we implemented EOS of a 50-MHz-repetition-rate train of few-cycle MIR waveforms, with 1.9-W-average-power, 13.8-fs gate pulses spectrally cantered at 1.95 µm, using GaSe nonlinear crystals (Fig. 1, Extended Data Fig. 1, for detailed setup description see Methods). In contrast to EOS configured to simultaneously employ sum- and difference-frequency generation, which requires a thin crystal[35], here we optimized the efficiency of phase-matched upconversion[36] using sum-frequency generation[4,12,37]. To this end, both the carrier wavelength and the average power of the gate pulses were increased as compared to the most sensitive EOS implementations to date[12,35]. The long central wavelength favours increasing the crystal thickness without compromising broadband detection[15]. In addition, the reduced gate-pulse photon energy mitigates multi-photon absorption, allowing for gate-pulse intensities as high as 9×10^{10} W/cm^2 inside the EOS crystal, maximizing the upconversion efficiency.

Scanning the gate pulse over a delay range of 1.3 ps using a 541-µm-thick GaSe crystal as the EOS interaction medium resulted in the trace shown in black in Fig. 2A (time-dependent EOS-signal-to-detection-noise ratio, SDNR). The detection noise (inset) is dominated by the gate-pulse shot noise in the balanced detection[38] and was measured for an integration time of 1 s per temporal element, see also Methods). At the delay of maximum absolute power depletion, the fraction of converted MIR photons ($\eta_{\text{conversion}}$) was 22% (Fig. 2B). Because only a portion of the MIR wave (Extended Data Fig. 3) interacts with the gate pulse upon propagation through the crystal ($\eta_{\text{interaction}}$, indicated by shaded area), we estimate a depletion of $\eta_{\text{conversion}}/\eta_{\text{interaction}} = 31\%$ within the temporal gate. For this delay, Fig. 2C shows the generated sum-frequency signal. Its power matches the MIR power depletion in terms of number of photons, thus allowing us to exclude other possible mechanisms of significant MIR depletion. The spectral filters employed to optimize the SDNR[39] have a transmission η_{BPF}. Selecting this spectral band for balanced heterodyne detection[12,36] reduced the fraction of detectable MIR photons from within the temporal gate to $\eta_{\text{total}} \approx 7.5\%$. This spectrally-integrated photon detection efficiency is consistent with the value determined from the ratio of the peak SDNR of the EOS trace to that of the MIR photon rate on the EOS crystal (see also Methods).

Fig. 2D shows the spectrally-resolved detection efficiency (right y-axis) obtained from the EOS spectra (left y-axis), assuming delay-independence of η_{total} (confirmed in Extended Data Fig. 4, see also Methods). It peaks at ~17% and exceeds 1% in the 900-to-1270 cm^{-1} range. The measurement noise floor (Fig. 2A, inset) indicates a minimum measurable field strength of 2.2 mV/cm (dashed line). This limit is calculated for our MIR beam radius of 35 µm at the detection crystal. For comparison, this value is only a factor of ~4 above the ultimate limit achievable with an ideal EOS detection capturing all MIR photons within the temporal gate.

The shape and duration of the temporal gate (Extended Data Fig. 3) and, therefore, the temporal resolution (or, the detection bandwidth), as well as the upconversion efficiency, result from a complex interplay of the experimental parameters[36]. These include crystal thickness and orientation, gate-pulse power, bandwidth and chirp, as well as focusing geometry and spectral filters. In fact, the demonstrated upconversion efficiency, in combination with lower-noise gate pulses would enable a peak detection efficiency exceeding 50% (see Supplementary Information section III). A more uniform spectral coverage at the expense of a lower detection efficiency was achieved employing a thinner EOS crystal. In this case the spectral range for $\eta_{\text{total}} > 1\%$ is nearly doubled (Extended Data Fig. 5 and Extended Data Table 3).

Field-resolved spectroscopy of gases

The instrument response of both crystals is sufficiently broadband for the EOS traces to qualitatively reproduce the temporal evolution of the super-octave electric field (Fig. 2A, red, Extended Data Figs. 5,6) which reaches MV/cm levels. Under the assumption of a linear instrument response, precise knowledge of the MIR electric field evolution is not necessary for quantitative, linear spectroscopy[12]. To confirm this assumption and to put the detection sensitivity and dynamic range to the test in a spectroscopy experiment, we recorded EOS traces of gas samples.

The 45-cm-long gas cell was first filled with methanol at concentrations between the vapour pressure (11% = 1.1×10^8 ppb) and the lower ppb range (Extended Data Fig. 7). Fig. 3A shows the envelope of time-domain EOS traces. Empty-cell EOS measurements allow for a quantitative comparison of the molecular response with the HITRAN line-by-line database[40,41], see also Methods.

The reference measurement (that is, the difference of two empty-cell EOS traces, Fig. 3A, black dotted line) shows that roughly 3 ps after the excitation maximum, detection-noise-limited sensitivity is approached within a factor of 3. Evaluating the methanol Q-branch signal in the 3-ps-to-9.8-ps time window after subtraction of the separately-measured empty-cell response yields excellent agreement with the HITRAN-based model for concentrations below 1000 ppm

(Fig. 3B). A noise-equivalent limit of detection (LOD) of 0.8 ppb is obtained (Fig. 3B, brown line). Near vapour pressure, strong modulations of the leading part of the sample response are observed. To ensure that these can be solely attributed to the linear refractive index of the sample, we measured the response of two high concentrations (0.5% and 11%) at a 100-times weaker excitation power (Fig. 3A, left, dashed lines, Extended Data Figs. 8,9). The accordance of the respective sample responses confirms the linearity both of the light-matter interaction and of the instrument response within our measurement accuracy, see also Methods and Extended Data Fig. 10. Thus, linear detection of methanol vibrations over a range of concentrations spanning 8 orders of magnitude was confirmed (Fig. 3C).

To showcase the benefit of broadband detection, we investigated a mixture of methanol, acetylene and methane, whose absorption spectra encompass more than one octave in the molecular fingerprint region. The Fourier transformations of time-filtered EOS traces along with corresponding HITRAN-based simulations are shown in Fig. 4A. The excellent agreement between experiment and model corroborates the ability of our instrument to perform broadband quantitative measurements, and predicts simultaneous LOD values of 0.8 ppb, 0.6 ppb and 40 ppb for methanol, acetylene and methane, respectively.

Conclusions and outlook

In conclusion, we have demonstrated sampling of super-octave long-wave mid-infrared electric fields with sensitivities approaching the ultimate limit set by the detection of all infrared photons within the temporal gate. For our geometry, this implies the ability to measure MIR electric-field strengths in the few-mV/cm range, with detection linearity preserved up to the MV/cm field-strength range. As a direct implication of far-reaching importance, we have demonstrated quantitative, super-octave molecular vibrational spectroscopy of gases, with concentrations spanning 8 orders of magnitude. The limit of detection, evaluated in terms of noise-equivalent absorbance, exceeds that of state-of-the-art broadband infrared vibrational spectroscopies[13,32,42,43] by more than one order of magnitude (Extended Data Table 4). The presented instrumentation will yield detectable concentrations well into the lower (or even sub-) ppt range by means of path-length elongation (Fig. 4B) with, e.g., multi-pass cells[32] or enhancement cavities[44,45].

This new regime of detection sensitivity and dynamic range, together with its power scalability opens new perspectives for ultrafast optical spectroscopy. Quantitative, label-free breath gas analysis with ppt-level sensitivity, used for identifying and monitoring infectious diseases[23] and cancer[46] are prominent examples addressing yet unmet medical needs.

References:

1. Valdmanis, J. & Mourou, G. Subpicosecond electrooptic sampling: Principles and applications. *IEEE J. Quantum Electron.* **22**, 69–78 (1986).
2. Wu, Q. & Zhang, X. -C. Free-space electro-optic sampling of terahertz beams. *Applied Physics Letters* **67**, 3523–3525 (1995).
3. Leitenstorfer, A., Hunsche, S., Shah, J., Nuss, M. C. & Knox, W. H. Detectors and sources for ultrabroadband electro-optic sampling: Experiment and theory. *Appl. Phys. Lett.* **74**, 1516–1518 (1999).
4. Kübler, C., Huber, R., Tübel, S. & Leitenstorfer, A. Ultrabroadband detection of multi-terahertz field transients with GaSe electro-optic sensors: Approaching the near infrared. *Appl. Phys. Lett.* **85**, 3360–3362 (2004).
5. Keiber, S. *et al.* Electro-optic sampling of near-infrared waveforms. *Nature Photonics* **10**, 159–162 (2016).
6. Ridente, E. *et al.* Electro-optic characterization of synthesized infrared-visible light fields. *Nat Commun* **13**, 1111 (2022).
7. Alqattan, H., Hui, D., Sennary, M. Y. S. & Hassan, M. Attosecond electronic delay response in dielectric materials. *Faraday Discuss.* 10.1039.D2FD00002D (2022).
8. Smith, P. R., Auston, D. H. & Nuss, M. C. Subpicosecond photoconducting dipole antennas. *IEEE J. Quantum Electron.* **24**, 255–260 (1988).
9. Sederberg, S. *et al.* Attosecond optoelectronic field measurement in solids. *Nat Commun* **11**, 430 (2020).
10. Itatani, J. *et al.* Attosecond Streak Camera. *Physical Review Letters* **88**, (2002).
11. Kienberger, R. *et al.* Atomic transient recorder. *Nature* **427**, 817–821 (2004).

12. Pupeza, I. *et al.* Field-resolved infrared spectroscopy of biological systems. *Nature* **577**, 52–59 (2020).

13. Kowligy, A. S. *et al.* Infrared electric field sampled frequency comb spectroscopy. *Sci. Adv.* **5**, eaaw8794 (2019).

14. Butler, T. P. *et al.* Watt-scale 50-MHz source of single-cycle waveform-stable pulses in the molecular fingerprint region. *Optics Letters* **44**, 1730 (2019).

15. Hofer, C. *et al.* Electro-Optic Sampling with Percent-Level Detection Efficiency. in *2021 Conference on Lasers and Electro-Optics Europe & European Quantum Electronics Conference (CLEO/Europe-EQEC)* 1–1 (IEEE, 2021).

16. Gaida, C. *et al.* Watt-scale super-octave mid-infrared intrapulse difference frequency generation. *Light: Science & Applications* **7**, (2018).

17. Elu, U. *et al.* Seven-octave high-brightness and carrier-envelope-phase-stable light source. *Nat. Photonics* **15**, 277–280 (2021).

18. Vasilyev, S. *et al.* Super-octave longwave mid-infrared coherent transients produced by optical rectification of few-cycle 25-μm pulses. *Optica* **6**, 111 (2019).

19. Täschler, P. *et al.* Femtosecond pulses from a mid-infrared quantum cascade laser. *Nat. Photon.* **15**, 919–924 (2021).

20. Ru, Q. *et al.* Two-octave-wide (3–12 μm) subharmonic produced in a minimally dispersive optical parametric oscillator cavity. *Opt. Lett.* **46**, 709 (2021).

21. Catanese, A. *et al.* Mid-infrared frequency comb with 67 W average power based on difference frequency generation. *Opt. Lett.* **45**, 1248 (2020).

22. Steinleitner, P. *et al.* Single-cycle infrared wavform control. *Nature Photonics, in press* (2022). DOI: 10.1038/s41566-022-01001-2

23. Ahmed, W. M., Lawal, O., Nijsen, T. M., Goodacre, R. & Fowler, S. J. Exhaled Volatile Organic Compounds of Infection: A Systematic Review. *ACS Infect. Dis.* **3**, 695–710 (2017).
24. Amann, A. & Smith, D. *Volatile Biomarkers*. (Elsevier, 2013).
25. Demtröder, W. *Molecular Physics*. (Wiley-VCH Verlag GmbH, 2005).
26. Sell, A., Scheu, R., Leitenstorfer, A. & Huber, R. Field-resolved detection of phase-locked infrared transients from a compact Er:fiber system tunable between 55 and 107 THz. *Applied Physics Letters* **93**, 251107–1 (2008).
27. Griffiths, P. R. & De Haseth, J. A. *Fourier transform infrared spectrometry*. (Wiley-Interscience, 2007).
28. Newbury, N. R., Coddington, I. & Swann, W. Sensitivity of coherent dual-comb spectroscopy. *Optics Express* **18**, 7929 (2010).
29. Foltynowicz, A., Ban, T., Masłowski, P., Adler, F. & Ye, J. Quantum-Noise-Limited Optical Frequency Comb Spectroscopy. *Physical Review Letters* **107**, (2011).
30. Rogalski, A. Next decade in infrared detectors. in *Electro-Optical and Infrared Systems: Technology and Applications XIV* (eds. Huckridge, D. A., Ebert, R. & Bürsing, H.) 100 (SPIE, 2017).
31. Lesko, D. M. B. *et al.* A six-octave optical frequency comb from a scalable few-cycle erbium fibre laser. *Nat. Photonics* **15**, 281–286 (2021).
32. Muraviev, A. V., Smolski, V. O., Loparo, Z. E. & Vodopyanov, K. L. Massively parallel sensing of trace molecules and their isotopologues with broadband subharmonic mid-infrared frequency combs. *Nature Photonics* **12**, 209–214 (2018).
33. Schwaighofer, A. *et al.* Beyond Fourier Transform Infrared Spectroscopy: External Cavity Quantum Cascade Laser-Based Mid-infrared Transmission Spectroscopy of Proteins in the Amide I and Amide II Region. *Analytical Chemistry* **90**, 7072–7079 (2018).

34. Hofer, C. *et al.* Mid-infrared electric field sampling approaching single-photon sensitivity. *EPJ Web Conf.* **243**, 16001 (2020).

35. Riek, C. *et al.* Direct sampling of electric-field vacuum fluctuations. *Science* **350**, 420–423 (2015).

36. Gallot, G. & Grischkowsky, D. Electro-optic detection of terahertz radiation. *Journal of the Optical Society of America B* **16**, 1204 (1999).

37. Liu, K., Xu, J. & Zhang, X.-C. GaSe crystals for broadband terahertz wave detection. *Appl. Phys. Lett.* **85**, 863–865 (2004).

38. Hobbs, P. C. D. Ultrasensitive laser measurements without tears. *Applied Optics* **36**, 903 (1997).

39. Porer, M., Ménard, J.-M. & Huber, R. Shot noise reduced terahertz detection via spectrally postfiltered electro-optic sampling. *Optics Letters* **39**, 2435 (2014).

40. Gordon, I. E. *et al.* The HITRAN2020 molecular spectroscopic database. *Journal of Quantitative Spectroscopy and Radiative Transfer* **277**, 107949 (2022).

41. Kochanov, R. V. *et al.* HITRAN Application Programming Interface (HAPI): A comprehensive approach to working with spectroscopic data. *Journal of Quantitative Spectroscopy and Radiative Transfer* **177**, 15–30 (2016).

42. Timmers, H. *et al.* Molecular fingerprinting with bright, broadband infrared frequency combs. *Optica* **5**, 727 (2018).

43. Phillips, M. C., Myers, T. L., Johnson, T. J. & Weise, D. R. In-situ measurement of pyrolysis and combustion gases from biomass burning using swept wavelength external cavity quantum cascade lasers. *Opt. Express* **28**, 8680 (2020).

44. *Cavity-Enhanced Spectroscopy and Sensing*. vol. 179 (Springer Berlin Heidelberg, 2014).

45. Winkler, G. *et al.* Mid-infrared interference coatings with excess optical loss below 10 ppm. *Optica* **8**, 686 (2021).

46. Maiti, K. S. *et al.* Towards reliable diagnostics of prostate cancer via breath. *Sci Rep* **11**, 18381 (2021).

47. Gerz, D. *et al.* Mid-infrared long-pass filter for high-power applications based on grating diffraction. *Opt. Lett.* **44**, 3014 (2019).

48. Sulzer, P. *et al.* Determination of the electric field and its Hilbert transform in femtosecond electro-optic sampling. *Phys. Rev. A* **101**, 033821 (2020).

49. Tomasino, A. *et al.* Wideband THz Time Domain Spectroscopy based on Optical Rectification and Electro-Optic Sampling. *Sci Rep* **3**, 3116 (2013).

50. Linstrom, P. NIST Chemistry WebBook, NIST Standard Reference Database 69, retrieved March 31, 2022.

Acknowledgments:

We thank Alexander Apolonski, Liudmila Voronina, Philipp Sulzer for useful discussions.

Funding:

IMPRS-APS Graduate School (DG, CH)

Max-Planck School of Photonics (DG)

Technology Transfer Program of the Max Planck Society (MH, EF)

Max Planck-UBC-UTokyo Center for Quantum Materials (MH)

Research project “SARSCoV2Dx” (13N15742), German Federal Ministry of Education and Research, within the funding program Photonics Research Germany

Author contributions:

Conceptualization: CH, DG, FK, IP

Data curation: CH, DG

Formal Analysis: CH, DG, LF, MHö

Supervision: JL, FK, IP

Investigation: CH, DG, LF, TB, MG, TH, CG, KM, MHu, EF

Visualization: DG, CH

Methodology: CH, DG, LF, MHö, KM, MHu, EF

Project administration: IP

Writing – original draft: CH, DG, IP

Writing – review & editing: all authors

Competing interests: Authors declare that they have no competing interests.

Data and materials availability: All data in the main text or the supplementary materials is available from the authors upon reasonable request.

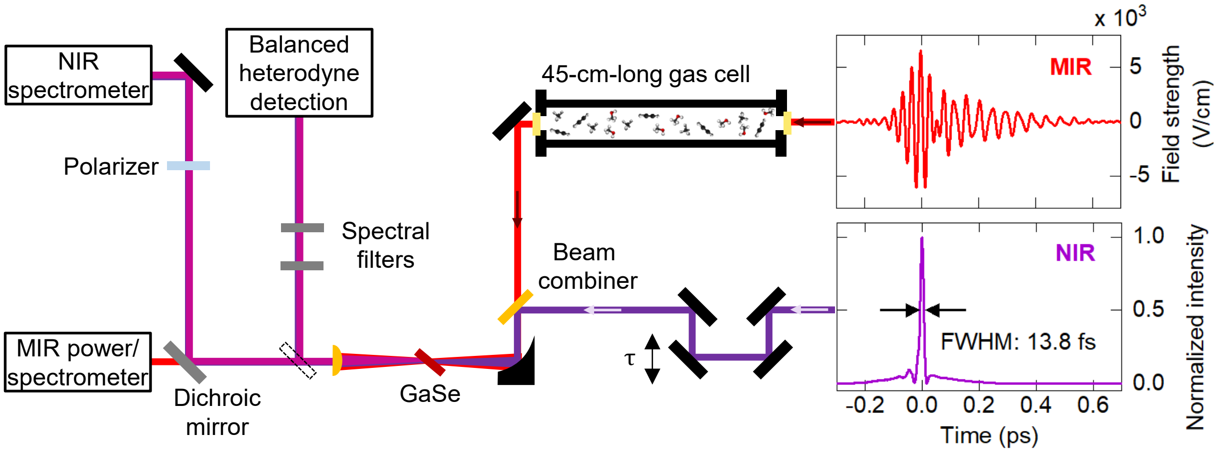

Fig. 1. Schematic of the experiment. Detailed in Methods and Extended Data Fig. 1. Measurement of the photon detection efficiency (without the dashed-line-framed mirror and with evacuated sample cell): a train of waveform-stable, few-cycle mid-infrared (MIR) pulses (red waveform) is focused collinearly with the variably-delayed (τ) train of near-infrared (NIR), 13.8-fs full-width-at-half-intensity-maximum (FWHM) gate pulses (purple intensity envelope) onto the EOS crystal (GaSe). The spectrally-integrated MIR average power and the NIR spectrum are recorded as functions of τ. Gas spectroscopy configuration (with the dashed-line-framed mirror and filled cell): MIR pulses excite molecular vibrations in a gas. The resulting coherent field oscillations are sampled electro-optically using the variably-delayed NIR gate pulses and a balanced heterodyne detection setup including spectral filters[39].

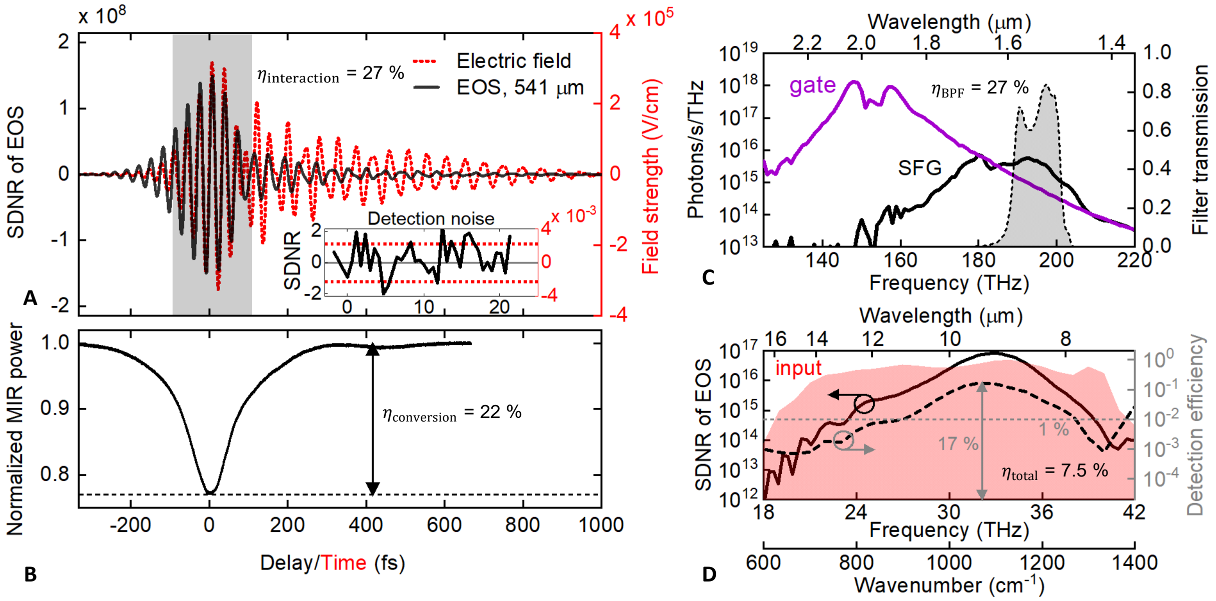

Fig. 2. Characterisation of EOS detection sensitivity and dynamic range. (**A**) 1.3-ps-long EOS trace with 2240 data points (temporal elements), EOS-signal-to-detection-noise ratio SDNR (black). Red, dotted on right y-axis: retrieved electric-field at the EOS crystal (see also Methods and Extended Data Fig. 2). Shaded area: estimated duration of the temporal gate, related by $\eta_{\text{interaction}}$ to the total flux of MIR photons per second. Inset: detection noise measurement (blocked MIR) for 1-s integration time per temporal element. Dotted lines: minimum measurable field strength (at SDNR=1). (**B**) Spectrally-integrated MIR power measured behind the EOS crystal (see Fig. 1), using the same time axis as in (A), $\eta_{\text{conversion}}$: MIR to sum-frequency conversion efficiency measured at maximum depletion. (**C**) Sum-frequency signal (black) between MIR wave and gate pulses (purple, blocked MIR beam), recorded at maximum MIR depletion, and filter transmission (grey area, η_{BPF}). (**D**) Red area: MIR spectrum impinging on the EOS crystal (at arbitrary logarithmic scale), measured with a Fourier-transform spectrometer. Left y-axis/continuous line: EOS spectral-intensity SDNR obtained from the full scan shown in (A), scales linearly with measurement time[12]. Right y-axis/dashed line: spectrally resolved

detection efficiency (independent on measurement time), calculated as the ratio of the EOS spectra and the MIR spectrum (red), normalized to the spectrally-integrated detection efficiency $\eta_{\mathrm{total}} = \eta_{\mathrm{conversion}}/\eta_{\mathrm{interaction}} \times \eta_{\mathrm{BPF}} \times \eta_{\mathrm{Fresnel}}$, which includes Fresnel-reflection losses at the GaSe crystal ($\eta_{\mathrm{Fresnel}} = 0.87$), see also Methods. Grey dashed line indicates 1 % detection efficiency.

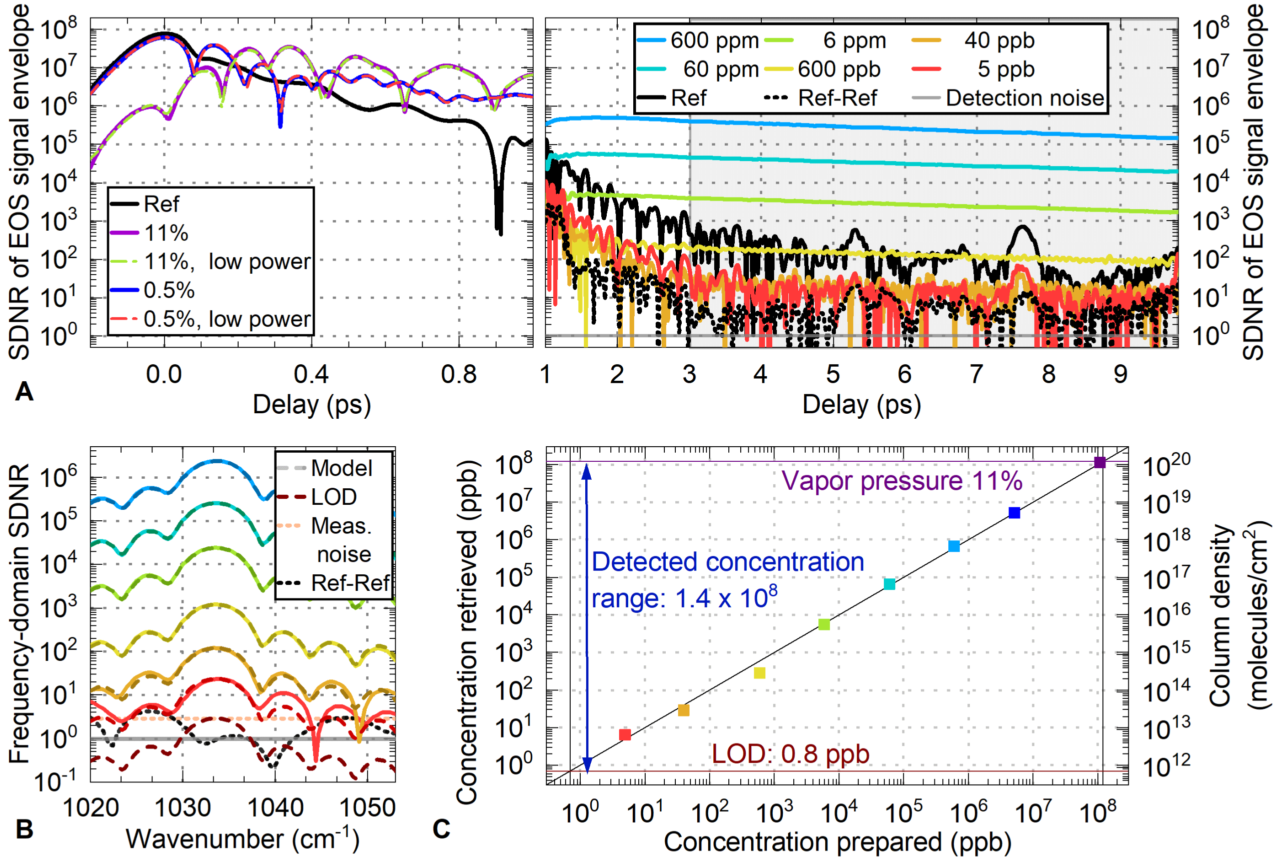

Fig. 3. Field-resolved spectroscopy of methanol. (**A**) envelopes of time-domain EOS traces, normalized to the single-scan detection-noise level. Black line: reference waveform (empty gas cell). Left panel: reference and sample response for percent-level concentrations with excitation powers of 19 mW in a 6-mm $1/e^2$-intensity-diameter beam at the sample (12 mW reaching the EOS crystal, solid line) and ~100 times lower power (dashed line). Right panel: differences between sample-response and empty-cell reference measurements. Individual 10.6-ps-long traces were acquired in a total measurement time of 80 seconds per trace. (B) solid lines: magnitude of the Fourier transforms of the signals in A, in the 3-ps-to-9.8-ps time window. Dashed lines: HITRAN model. (**C**) retrieved versus prepared concentration. See Methods for details on sample preparation, signal acquisition, processing, and concentration retrieval.

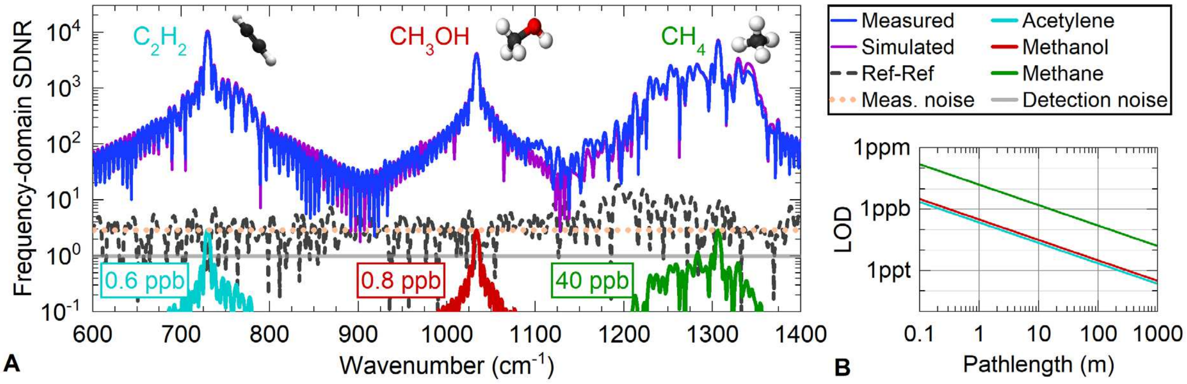

Fig. 4. Broadband spectroscopy of a mixture of methanol, acetylene and methane. (**A**) Blue: scaled magnitude of the Fourier-transform of the 3-to-9.8-ps time window after subtracting an empty-cell measurement from the sample response. Purple: sample response simulated using our measured excitation, HITRAN line-by-line data[41] and fit parameters for the concentration of the three gases: 0.9 ppm, 4.1 ppm and 84.4 ppm for methanol, acetylene and methane, respectively. Black, dashed: magnitude of the Fourier-transform of the difference of two empty-cell EOS measurements. Beige: measurement noise floor obtained from the mean of the black, dashed line. Grey: detection noise. Simulated spectra of the measurement-noise-equivalent LOD concentrations are shown. (**B**) LOD for methanol, acetylene and methane extrapolated with respect to the interaction length.

Methods

Description of the experimental setup

The employed instrument is an adapted implementation of the system described in detail in Ref.[14]. The setup is depicted in Extended Data Fig. 1. The pulsed output of an erbium fibre oscillator (Menlo C-fibre), operating at a wavelength of 1.5 µm and a repetition rate of 100 MHz, is pulse-picked down to 50 MHz, amplified and shifted to 2 µm in a highly nonlinear fibre. A chirped fibre Bragg grating cuts out a spectrum around 1965 nm resulting in stretched pulses with 500 ps pulse duration. This pulse train seeds a two-stage thulium-doped fibre amplifier and delivers, after a free-space grating compressor, near-infrared (NIR) pulses with a full-width-at-half-intensity maximum (FWHM) duration of 250 fs. Starting at the grating compressor, the free-space beam path is enclosed in a vacuum chamber (<10^{-3} mbar) to avoid absorption from gases such as water vapor, thus ensuring minimal background from molecules outside the measurement cell. The beam is split in two and the pulses are further compressed in silica photonic crystal fibres. Sampling pulses for electro-optic sampling (EOS) are nonlinearly self-compressed in a large mode area fibre (LMA15 from NKT Photonics) down to a FWHM duration of 13.8 fs with an average power of 4.5 W. For mid-infrared (MIR) generation, the NIR pulses are compressed down to durations of 32 fs FWHM with 30 W of average power in a large-pitch-fibre (LPF40 fibre). Intra-pulse difference frequency generation (IPDFG) in a 1-mm-thick gallium selenide (GaSe) crystal results in waveform-stable MIR pulses with 250 mW average power and an intensity spectral coverage between 630 cm^{-1} and 1370 cm^{-1} at the -20-dB-level. As compared to the original implementation in Ref.[14], here we operate the system at a safe level below its power record. Grating-based long pass filters (LPF) separate the MIR pulses from the pump [47] before the MIR beam is mechanically chopped at a frequency of 10 kHz. The MIR beam passes a home-built, 45-cm-long measurement cell with 1-mm-thick ZnSe windows. A 10-mm-thick germanium substrate compensates the second-order dispersion of ZnSe. A 1-mm-thick ZnSe substrate placed at Brewster angle recombines the sampling pulses (s-polarization, in reflection) and the MIR pulses (p-polarization, in transmission). The sampling beam is transverse-mode-matched to the MIR beam via a reflective telescope. It is variably delayed for EOS measurements with a mechanical stage, whose displacement is tracked with a Michelson interferometer (SmarAct Picoscale). The collinearly propagating beams are focused into a GaSe crystal with average powers of 1.9 W and 12 mW for the sampling and MIR pulses, respectively. The EOS crystal phase-matches p-polarized sum frequency generation (SFG). After a 1500-1600 nm bandpass filter, the NIR beam is split in two orthogonal polarizations by a Wollaston prism, followed by a balanced detector with two InGaAs diodes. By adjusting a quarter-wave plate and a half-wave plate before the Wollaston prism, close to shot-noise-limited detection (factor ~1.4) is achieved at the chopping frequency of 10 kHz, with a lock-in amplifier using an integration time of 2.2 ms. This ellipsometer detects the SFG field in a heterodyne fashion.

Electro-optic sampling and detection efficiency

The EOS traces were acquired with an integration time of 2.2 ms per temporal element. For calculation of the detection efficiency via the photon flux, the signal-to-detection-noise ratio (SDNR) is shown for an effective averaging time of 1 s per temporal element. To that end, noise traces were acquired for 1s, the averages and standard deviation resulting in the noise measurement shown in Fig. 2A and Extended Data Fig. 5. Linear scaling of the intensity SDNR with for integration times up to 1600 s was previously shown[12].

To relate the time-domain SDNR to the detection efficiency, we first calculate the MIR photon flux as a function of time (i.e., delay) from the pulse energy and electric field distribution.

For the given time-domain instrument response, the photons in the interaction time window at the delay of maximum signal strength are then estimated. The ratio of the SDNR to the photon flux then gives the overall detection efficiency. This includes effects which are not considered by the calculation of MIR depletion and spectral filtering, e.g., spectrally varying phase relations between the sum-frequency and local oscillator components[48], as well as imperfect spatial interference. The result is an estimated overall average detection efficiency of 5.9 %.

The spectrally-resolved detection efficiency in Fig. 2D is calculated as follows: First, the area under the EOS spectrum is normalized to the overall detection efficiency η_{total}. Then, the ratio of the spectrum to the spectrally-resolved input photon flux (incident power of 12 mW (chopped) with Fresnel losses at the GaSe interface and FTIR spectrum) results in the detection efficiency. This calculation neglects the remaining chirp of the MIR waveform, as it assumes a constant spectral distribution equal to that of the FTIR spectrum (i.e. a Fourier-transform limited MIR field) and, correspondingly, a constant spectrally integrated relative depletion throughout the entire EOS trace.

The MIR focus size was chosen for optimum spatial overlap with the gate beam[49]. For a constant detection efficiency and integration time window, i.e. the same required minimum MIR photon flux per second, the minimum measurable field strength scales as follows: Increasing both the MIR and gate beam foci in the EOS crystal by a factor of 2 (to ensure spatial overlap) halving the minimum measurable field strength. To still achieve the required conversion efficiency, would need the gate pulse power to be increased by a factor of 4.

Gas sample preparation

The gas handling setup is shown in Extended Data Fig. 7. For the preparation of the gas samples, small amounts of the substance are injected with a gas tight syringe into an evacuated

($<10^{-1}$ mbar) gas sampling bulb. The gas sampling bulb with the sample gas (acetylene, methane and/or evaporated methanol) is then filled with nitrogen up to atmospheric pressure. Varying amounts of this stock solution are further diluted by injection via gas-tight syringes and septa into a 250-ml syringe filled with nitrogen. Via a three-way valve, the connection to a previously evacuated ($< 10^{-4}$ mbar) transport gas cell is opened and the atmospheric pressure on the piston leads to the filling of the transport cell. The transport cell is then connected to the measurement cell, which is evacuated ($< 10^{-2}$ mbar) and located in vacuum. Pressure equalization leads to a sample pressure of 84 mbar and further dilution. For methanol concentrations higher than 1000 ppm, a flask with liquid methanol is directly connected to the evacuated measurement cell. After removing the remaining gas in the flask with a vacuum pump, the liquid methanol evaporates and the pressure in the gas cell increases until reaching the vapor pressure of 110 mbar @ 19°C. For the 0.5% concentration measurement the pressure was reduced via repeated pressure equalization with an evacuated cell. For ease of comparison, the specified gas concentrations are given with respect to atmospheric pressure. For the gases used here, the signal strengths differ only by ~14 % when changing the total pressure from 84 mbar to 1 bar.

The gas cell components were cleaned between measurements by repeated nitrogen purging and evacuation of the gas cells to pressures below 1×10^{-2} mbar for several minutes. Prior to preparing the concentrations below 1 ppm all gas cell components were left over night in an oven at 60°C to remove remaining adsorbed molecules. However, for prepared methanol concentrations below 10 ppb, measurements revealed slowly increasing concentrations on timescales of minutes. The minimum preparable concentration was thus 5 ppb. This implies the need for more advanced sample preparation for low ppb and ppt concentrations such as constant gas flow setups.

Processing of spectroscopic data

For the gas-phase measurements, ten 10.6-ps-long EOS scans were averaged, each with a measurement time of 8 s. In order to circumvent the dynamic range limitations stemming from the utilized lock-in amplifier (MFLI, Zurich Instruments) and analog-to-digital converter (Picoscale, Smaract), ten additional scans with 100 times higher amplification of the transimpedance amplifier (DLPCA-200, FEMTO) were measured for the weak signals after the main pulse. The two averaged scans were serially stitched together at a time delay where the amplified scan wasn't saturated (typically starting around 1.5 ps). We refer to the result of this procedure as *one trace*. Thus, the effective measurement time of one trace is 80 s. Stitching can, in principle, be avoided by employing electronics with sufficient bit depths (26-bit) or fast scanning techniques (smaller integration time). In order to show the relevant signal and noise of the time-domain EOS traces, their envelopes presented in Fig. 3 are frequency-filtered with a cosine-squared filter, suppressing noise outside the spectral region of the excitation (500-1500 cm^{-1}). The traces are scaled to the mean of the detection noise (single trace, MIR blocked). In the following analysis, a reference trace (evacuated gas cell) is subtracted. For further isolation of the molecular signal from the excitation noise[12], a cosine-squared filter is applied in the time domain (3-9.8 ps). After padding the time-domain traces with zeros up to a delay of 100 ps, they are Fourier transformed and the real-valued magnitude is shown, normalized to the detection noise floor derived from a trace with the MIR beam being blocked (that is, the time-domain SDNR).

For quantitative concentration retrieval using a time-filtering approach, a model for the molecular response on the level of the electric field is necessary. To this end, we employ the line-by-line database from HITRAN to calculate the complex attenuation coefficient that includes the effects of temperature and pressure. The HITRAN Application Programming

Interface (HAPI)[41] provides for each absorption line *i* the parameters for a Lorentzian lineshape, namely the line strength (S_i), wavenumber (ν_i) and line width ($\Delta\nu_i$). The resulting attenuation coefficient μ can be used together with the path length *d* to calculate the transmission $T = \exp(-\mu \cdot d) = 10^{-A}$, where A is the decadic absorbance.

For the calculation of a complex Lorentzian L_c with these parameters, we use the following equation:

$$L_c(\nu, \nu_i, \Delta\nu_i) = \left(\Delta\nu_i - 1i(\nu - \nu_i)\right)/\pi\left((\nu - \nu_i)^2 + \Delta\nu_i{}^2\right)$$

In order to obtain a real-valued time-domain signal after the Fourier transformation, the complex conjugate of the values at negative frequencies is added. The complex attenuation coefficient is then defined by the sum over all absorption lines, scaled by their line strength:

$$\mu_c(\nu) = \sum_i S_i * \left(L_c(\nu, \nu_i, \Delta\nu_i) + L_c{}^*(-\nu, \nu_i, \Delta\nu_i)\right)$$

All relevant processes (sample interaction, EOS instrument response function) scale linearly with the MIR electric field. Therefore, the molecular response can be directly applied to the reference EOS trace to obtain the modelled sample EOS trace: $E_{\mathrm{sim}}(\nu) = E_{\mathrm{ref}}(\nu) \times \exp\left(-\frac{\mu_c(\nu)}{2} \cdot d\right)$. Note that for small attenuations of the excitation pulse ($\frac{\mu_c(\nu)}{2} \cdot d \ll 1$) the electric field envelope of the molecular response scales linearly with the number of emitters. As a consequence, it also scales linearly with the attenuation coefficient and the concentration, as can be seen in Fig. 3A and B. This scaling is derived in detail in the supplementary material of [12]. It differs from concentration retrievals based on intensity change such as in conventional FTIR spectroscopy, where the absorbance scales linearly with the concentration.

In the case of methanol and for our experimental settings, the assumption of a small attenuation breaks down for concentrations >1000 ppm, requiring an exact model of the molecular response for quantitative concentration retrievals. Extended Data Fig. 8 shows the frequency-domain SDNR of the 3-9.8 ps time window together with the modelled spectra for methanol concentrations of 0.5% and 11%. For 0.5%, the agreement is good, while for the higher concentration the model does not reproduce the measured signal, as two additional peaks arise around 960 cm^{-1} and 1080 cm^{-1}.

In order to ensure that we measure only the linear molecular response the measurements were repeated at a hundred times lower MIR power. Differences in the excitation (spectrum and intensity) are corrected using a calculated transfer function $H(\nu)= FT\{E_{ref}(t)\}/ FT\{E_{ref,low\ power}(t)\}$ and applying it to the trace measured at low power: $E_{sample,low\ power,corrected}(t) = IFT\{H(\nu)\cdot FT\{E_{sample,low\ power}(t)\}\}$. The resulting spectra of the time filtered traces are shown as dashed lines in Extended Data Fig. 8 and are in good agreement with the high-power data, confirming a linear measurement of the refractive index of the sample. These traces can be used as a calibration for the prepared methanol concentration and allows its retrieval in the future.

The reason for the difference of the measured and modelled spectra can be found in the comparison of the absorption spectra derived from the HITRAN database and from a FTIR measurement (PNNL database[50]), shown in Extended Data Fig. 9. The Q-, P- and R-branch of the C-O stretch band of methanol are in decent agreement, while outside of the spectral region of 870 –1100 cm^{-1} the HITRAN data approaches zero due to an incomplete set of absorption lines in the database. The PNNL data shows additional absorption features and an offset from zero. This difference has only a marginal influence in the case of small attenuations as the signal from the strongest absorption line (Q-branch absorption peak) dominates. For stronger absorbances (>1 AU) the abrupt end of the P and R-branch absorption line series gives rise to the peaks at 960

cm^{-1} and 1080 cm^{-1} in the modelled spectra. Other measured peaks can also be found in the PNNL data, e.g. at 736 cm^{-1}, 779 cm^{-1} or 821 cm^{-1}.

The concentration retrieval using the model described in the previous section can be successfully employed until either the uncertainties of the model or saturation effects start to majorly impact the analysis. In the non-depletion regime, the signal strength scales linearly with the concentration (Extended Data Fig. 10, red line). In our case, a deviation from linear scaling by 1% and 10% occurs at concentrations of 36 ppm and 370 ppm, respectively (Extended Data Fig. 10, yellow line). The signal increases monotonically up to 3000 ppm and follows a linear behavior over more than 5 orders of magnitude in concentration.

For absorbance measurements, the measurable range can be determined as described in Extended Data Table 1. The relative standard deviation δI of the intensity was determined from ten measurements to be 1.9×10^{-3}.

$$A_{\max} = -\log_{10}(\delta I) = 2.7\ AU$$

$$A_{\min} = \frac{\sqrt{2}}{\log(10)} \delta I = 1.2 \times 10^{-3}\ AU$$

The measurable absorbance range spans more than 3 orders of magnitude, corresponding to methanol concentrations between 2.5 ppm and 0.7%. Combining emission and absorption analysis for one spectral element derived from the same trace, the linear retrievable concentration range spans around 7 orders of magnitude in this spectral element (e.g., from 0.8 ppb to 0.7% for the spectral element centered at 1033.7 cm^{-1}). However, parallel and linear probing of a multitude of spectral elements, as enabled by broadband spectroscopy, increases the retrievable concentration range by more than one order of magnitude (see, e.g., resonances at 736 cm^{-1}, 779 cm^{-1} or 821 cm^{-1} in Extended Data Figs. 8,9).

Supplementary Information

I. Estimation for highly-multivariate detection within minutes

We assume an ideal light source and detection with negligible technical excess noise and detector noise. The detection limits are then set by shot noise. For the absorbance A, its uncertainty δA, the signal-to-noise ratio (SNR) and the photon numbers of the reference measurement, N_{ref} and the sample measurement N, we find:

$$A = -\log_{10}\left(\frac{N}{N_{\mathrm{ref}}}\right)$$

$$\delta A = \sqrt{\left(\left|\frac{dA}{dN}\right|\delta N\right)^2 + \left(\left|\frac{dA}{dN_{\mathrm{ref}}}\right|\delta N_{\mathrm{ref}}\right)^2}\text{ , with } \delta N = \sqrt{N}, \delta N_{\mathrm{ref}} = \sqrt{N_{\mathrm{ref}}}\,,$$

$$\delta A = \frac{1}{\ln(10)}\cdot\sqrt{\frac{1}{N}+\frac{1}{N_{\mathrm{ref}}}}\,,$$

$$SNR = \frac{A}{\delta A} = -\frac{\ln\left(\frac{N}{N_{\mathrm{ref}}}\right)}{\sqrt{\left(\frac{1}{N}+\frac{1}{N_{\mathrm{ref}}}\right)}}.$$

For large N_{ref} and $N \approx N_{\mathrm{ref}}$, that is, for low absorbance, the SNR can be approximated as

$$SNR \approx \frac{1-\frac{N}{N_{\mathrm{ref}}}}{\sqrt{\left(\frac{2}{N_{\mathrm{ref}}}\right)}}.$$

For SNR = 1, solving the above equation for N yields:

$$N_{\text{small A}} \approx N_{\mathrm{ref}} - \sqrt{2N_{\mathrm{ref}}}$$

For large absorbance, the smallest N, larger than or equal to its standard deviation and yielding SNR>1 is $N_{\text{large A}} = 1$. The measurable range of absorbances A_{range} is then given by

$$A_{\text{range}} \approx \frac{-\log_{10}\left(\frac{N_{\text{large A}}}{N_{\text{ref}}}\right)}{-\log_{10}\left(\frac{N_{\text{small A}}}{N_{\text{ref}}}\right)} = \frac{\ln(N_{\text{ref}})}{-\ln\left(1-\sqrt{\frac{2}{N_{\text{ref}}}}\right)}.$$

In accordance with the Beer-Lambert law, the measurable concentration range corresponds to the absorbance range. The number of photons available for a given power P, average time T, wavelength λ, speed of light c and Planck constant h is calculated as: $N_{ref} = \frac{P\lambda}{hc} T$.

The molecular fingerprint region is often defined as the spectral range between 2.5 µm and 20 µm (500-4000 cm^{-1}). Doppler-broadened lines of gases at room temperature have widths on the order of 0.001 cm^{-1}, resulting in around 3.5 million meaningful spectral bins. Assuming a laser source with 1 W of average power, a centre wavelength of 10 µm and an averaging time of 180 minutes, this results in a measurable concentration range per spectral bin of $> 10^{10}$. It should be noted that (i) the availability of the broadband absorption spectrum of a gaseous molecular species, consisting of a multitude of absorption lines with strongly varying strength[41], normally allows for a quantitative concentration retrieval surpassing the measurable concentration range in a single spectral bin by an order of magnitude or more. Furthermore, (ii) in many practical cases, a lower spectral resolution is sufficient. Both (i) and (ii) indicate the feasibility of quantitative molecular fingerprinting of complex gaseous samples, such as breath, with individual concentrations of ~10 orders of magnitude in a total averaging time of a few minutes.

II. Estimation of the detection efficiency in state-of-the-art field-resolved infrared spectroscopy

In Ref.[12], highest detection efficiency was achieved with a 500-µm-thick GaSe EOS crystal, amounting to a spectrally-averaged value of 0.5 % for an EOS measurement in the 970-to-1320-cm^{-1} band (at -30 dB intensity). In Ref.[13] , the authors claim a time-domain signal-to-noise ratio of 40, for a detection bandwidth of 50 MHz. With the stated mid-infrared power of 50 µW and central frequency of 39 THz, this corresponds to 4×10^7 photons within the integration time window. Attenuation by 40^2=1600 (to result in a SNR of 1) leads to 24000 photons within the integration time window, and an estimated 8000 photons within the interaction time window (MIR pulse duration: 29 fs, gate pulse duration: 10 fs), corresponding to a photon detection efficiency of 0.013%.

III. Estimation of the detection efficiency for gate pulses with lower intensity noise

The spectral filter in our experiment was empirically optimized for the best SDNR, while the theoretical optimum cut-off wavelength[39] would be at approximately 1700 nm, enabling transmission of more than 90 % of the generated sum-frequency photons. Increased intensity noise and diode saturation for higher local oscillator power/broader spectral ranges prevents us from balancing to the shot noise limit in such a filtering geometry and thus decreases the SDNR.

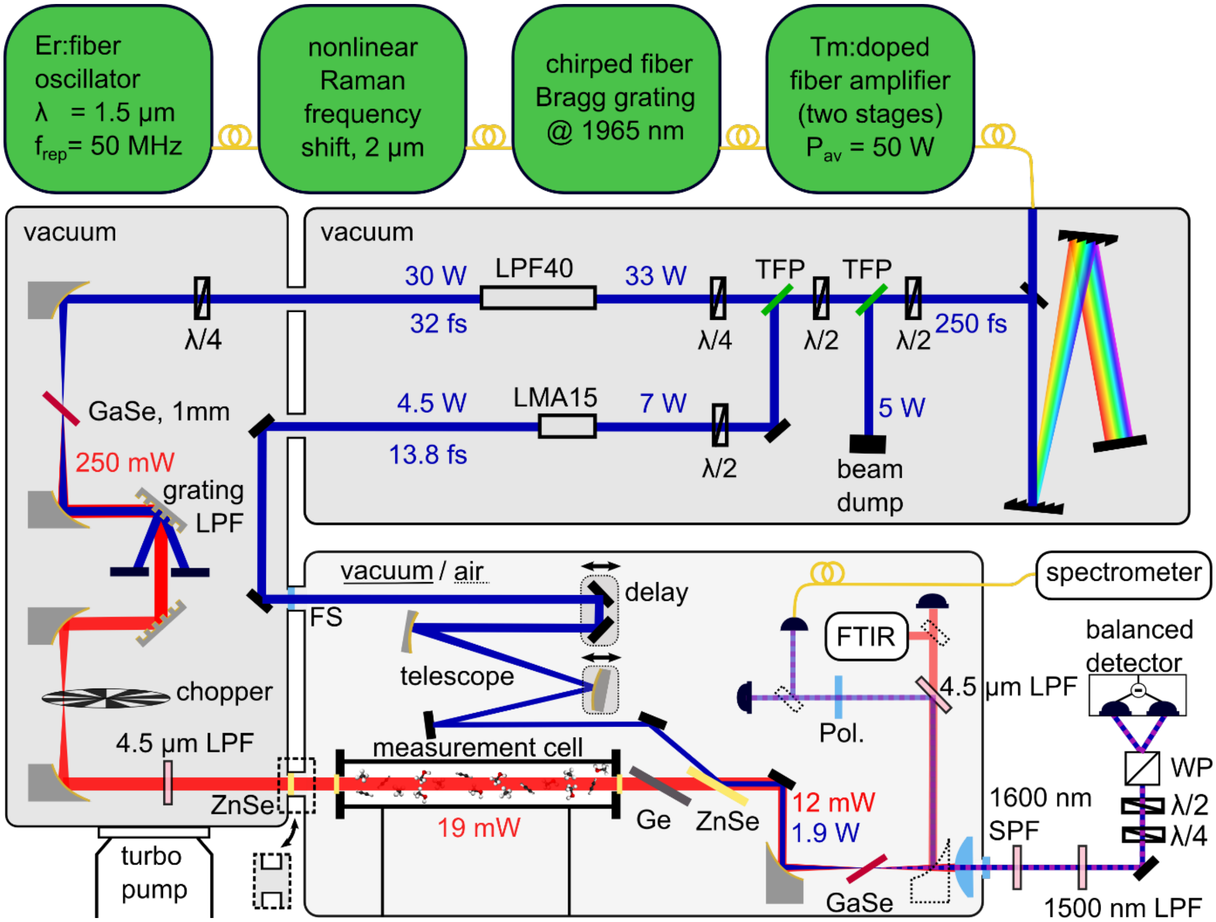

Extended Data Figure 1.

Detailed schematic of the optical setup. Er: erbium, Tm: thulium, TFP: thin-film polarizer, LMA15: a large mode area fibre, LPF40: a large-pitch fibre, λ/2: half-wave plate, λ/4: quarter-wave plate, GaSe: gallium selenide, LPF: long-pass filter, FS: fused silica, ZnSe: zinc selenide, Ge: germanium, SPF: short-pass filter, WP: Wollaston prism. The detection efficiency measurements were performed with the last chamber in air, with the ZnSe window between the chambers and the parabola after the EOS crystal inserted.

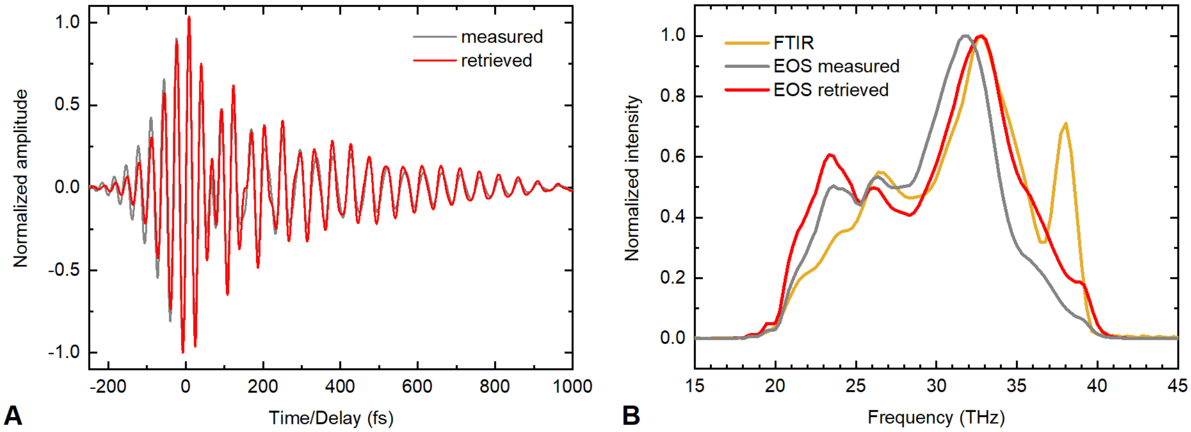

Extended Data Figure 2.

Estimated MIR electric field and EOS instrument response function for a 130-µm-thick GaSe crystal, ensuring a broadband spectral response and negligible spatial walk-off. (**A**) Measured EOS trace (grey), estimated MIR field retrieved using the calculated spectral response (red). (**B**) Measured (grey) and instrument-response-corrected (red) MIR spectra, as well as MIR spectrum measured with an FTIR spectrometer (orange). The instrument response function was calculated using a one-dimensional model for the EOS detection process, with the gate-pulse intensity envelope shown in Fig. 1 (purple, from second-harmonic generation frequency-resolved optical gating (FROG) measurement), the crystal geometry as determined from the experimental setup $(\Theta = 34^\circ, \varphi = 0^\circ)$ and the measured transmission for the 1500-1600-nm band-pass filter (Fig. 2C, right). The Fourier transform of the measured trace was then divided by the complex frequency-domain instrument response, yielding the red line in (B). This instrument response function incorporates phase matching, temporal walk-off, the gate-pulse properties and the effects of spectral filtering. It does not include spatial effects and gives no information on the carrier-envelope phase of the MIR waveform [48] (which is irrelevant for the experiments shown here). The waveform shown in Fig. 1 is obtained from the waveform shown in Fig. 2A and

Extended Data Fig. 2A (red lines), by numerically correcting for the spectral phase of 3-mm-thick ZnSe and 10-mm-thick Ge.

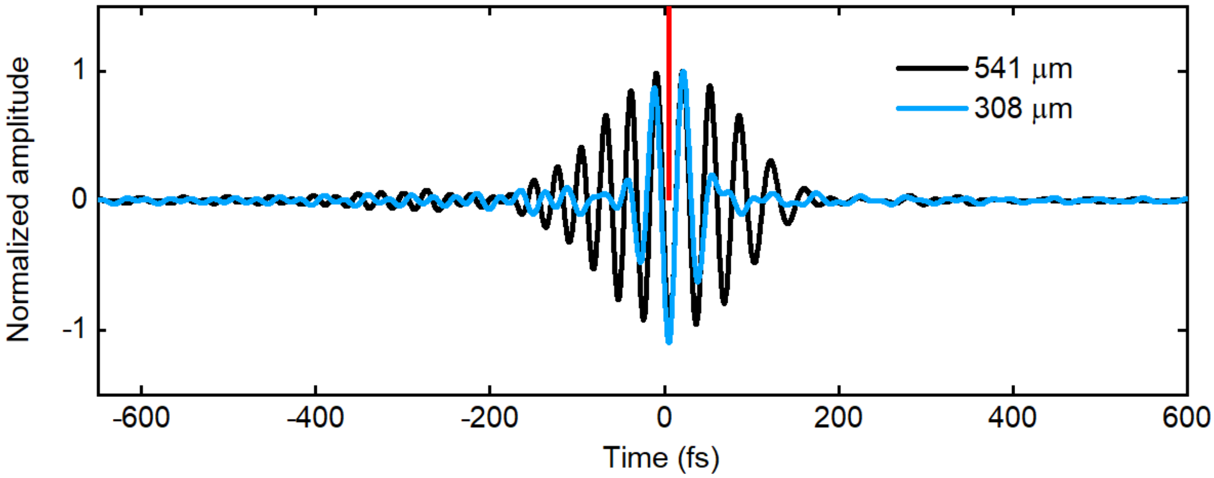

Extended Data Figure 3.

Temporal gate functions for the two detection crystal thicknesses, calculated as the Fourier transform of the respective complex spectral instrument response (complex ratio of the Fourier transforms of the incident field (Extended Data Fig. 2) and the EOS traces (Fig. 2A)). Multiplication by the complex frequency-domain instrument response corresponds to a convolution of the incident electric field with this (oscillating) time-domain gate function. The red line indicates the Dirac-delta-peak-like temporal response required for the theoretical limit of measuring exactly the electric field.

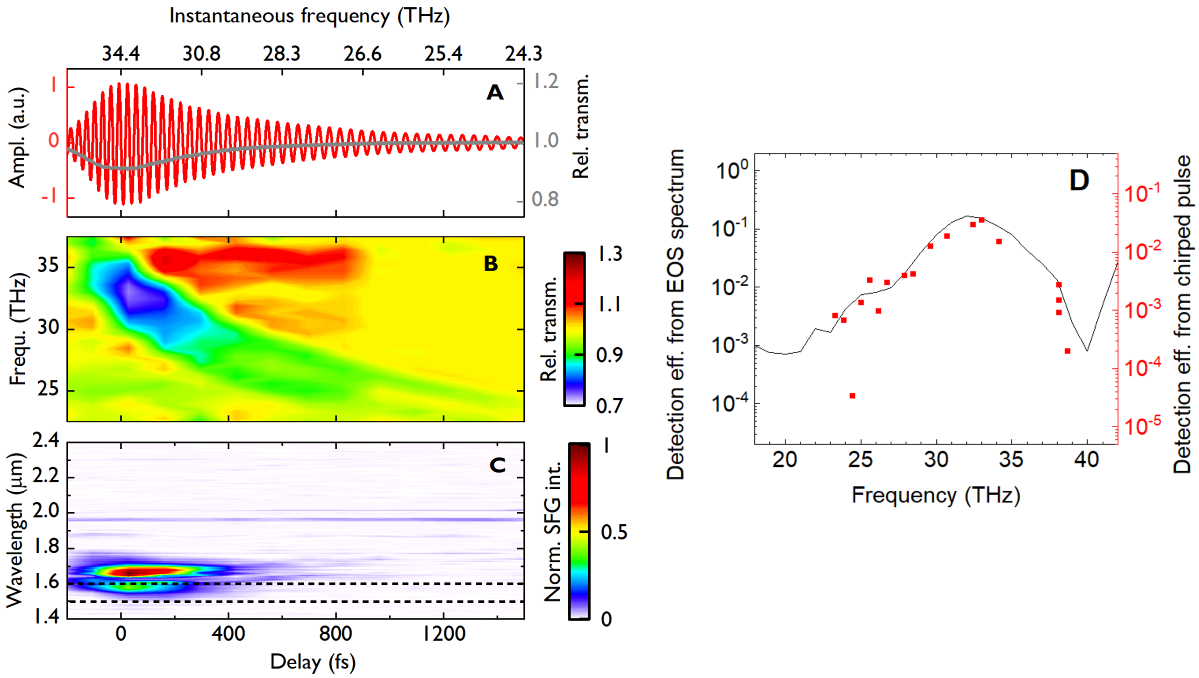

Extended Data Figure 4.

Determination of the spectrally-resolved detection efficiency from depletion measurements with a chirped MIR waveform. (**A**) EOS trace of the chirped MIR waveform (left axis) with instantaneous frequency (top x-axis) and spectrally-integrated power depletion measurement (right axis, grey). (**B**) Spectrally-resolved MIR depletion, measured with FTIR spectrometer. (**C**) Generated sum-frequency spectra, dashed lines indicating the spectral filtering region. (**D**) Frequency-dependent detection efficiency. Grey line, left y-axis: as in Fig. 2D. Red dots: calculated for the instantaneous frequencies in (A) and with the spectral filter transmission. While the spectral shapes agree well qualitatively, discrepancies in the quantitative values arise from a decreased number of interacting photons, as not all photons of one frequency are located at one delay.

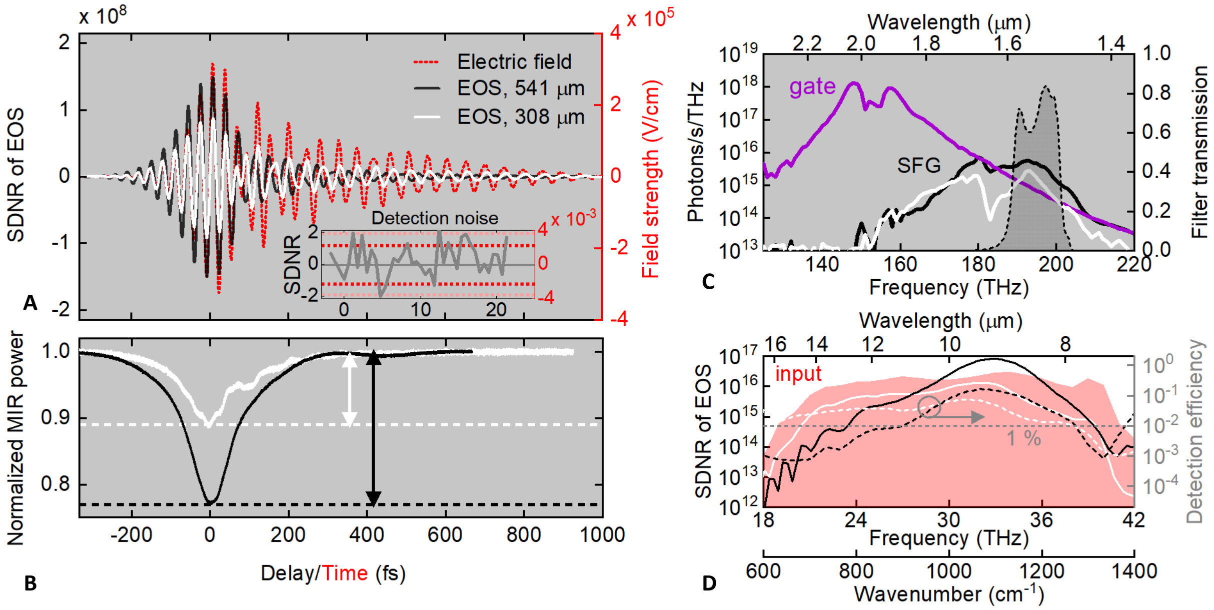

Extended Data Figure 5.

Comparison of the detection efficiency for two different detection crystal thicknesses. The black and red lines show the same results as in Fig. 2 in the various panels. The white lines are the results for a 308-µm-thick GaSe crystal. The corresponding efficiency values are summarized in Extended Data Table 3, together with the values for the 541-µm-thick crystal for comparison.

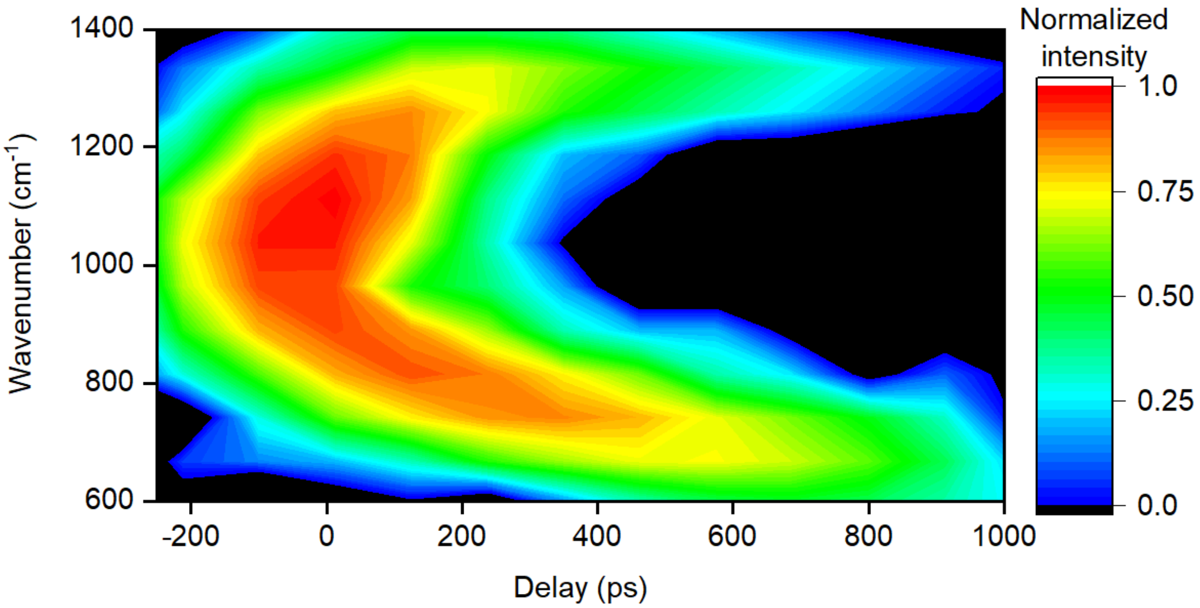

Extended Data Figure 6.

Spectrogram of the MIR waveform in Extended Data Fig. 2A, elucidating the remaining chirp of this waveform. The time-dependent amplitude of the EOS trace results from a combination of the frequency dependent detection efficiency and instantaneous spectrum. It thus decreases towards longer delays in comparison to the MIR waveform (Fig. 2A), where the chirp is combined with the reduced detection efficiency for longer MIR wavelengths (Fig. 2D).

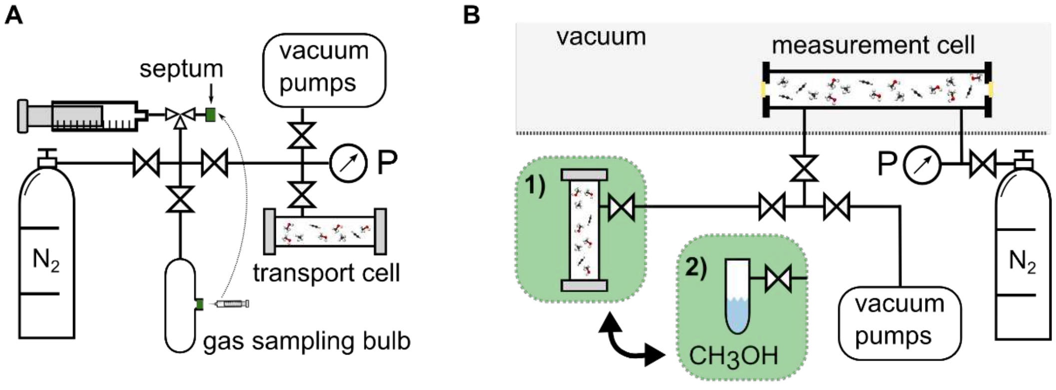

Extended Data Figure 7.

Gas handling setup (see also Methods). (**A**): preparation of low concentrations and gas mixtures in transport cell. (**B**): loading of measurement cell with 1) transport cell for low concentrations or gas mixtures and 2) high concentrations from evaporation.

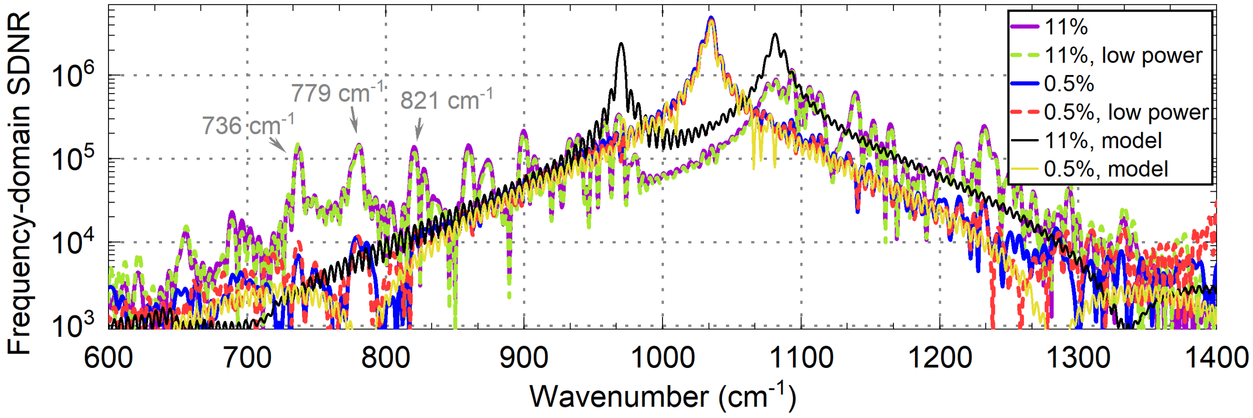

Extended Data Figure 8.

Frequency-domain magnitude of the 3-9.8 ps time window of modelled and measured EOS traces of methanol concentrations of 0.5% and 11%. Dashed lines: measured with 100 times lower MIR power and corrected using the transfer function H(ν).

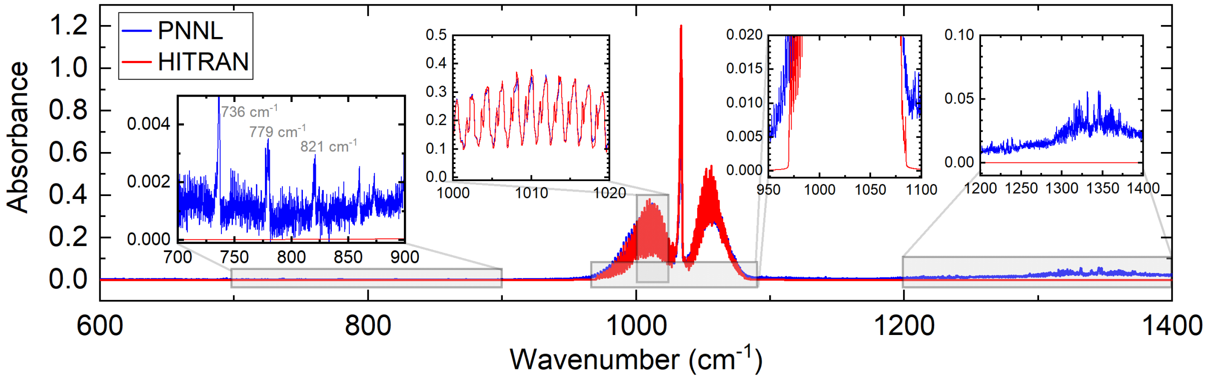

Extended Data Figure 9.

Comparison of the methanol absorbance (pressure: 1 atm (1013.25 mbar), path length: 1 m, concentration: 0.1 %, resolution 0.125 cm^{-1}, instrument response: boxcar) evaluated from transmission data in blue (PNNL) and from HAPI based on the HITRAN line-by-line database in red. Insets from left to right: absorbance peaks in PNNL which are absent in HITRAN; excellent agreement for P-branch; HITRAN model absorption line coverage (970-1085 cm^{-1}); broad absorbance feature in PNNL, absent in HITRAN.

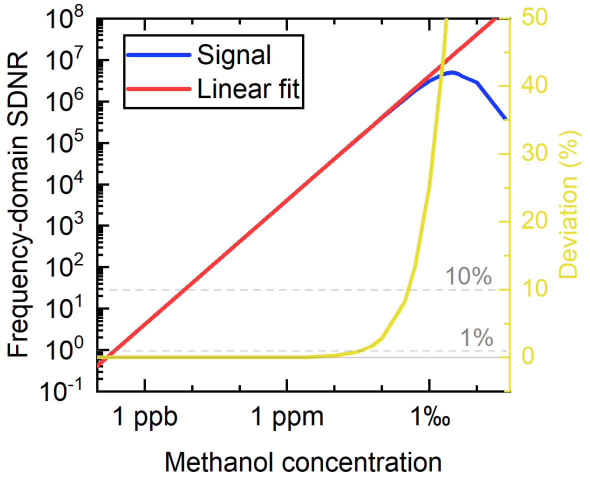

Extended Data Figure 10.

Simulated signal strength of the methanol (emission) peak (1033.7 cm^{-1}) of the Fourier transformed 3-9.8 ps time window. Red: result of linear fit using concentrations below 10 ppb. Yellow: relative deviation of the signal from the linear fit.

	Method	Intensity RMS noise	A_{min} [AU]	A_{max} [AU]	Dynamic range ($A_{\text{max}}/A_{\text{min}}$)
Ref. [13]	FRS ASOPS	0.013	$8.1\text{x}10^{-3}$	1.9	$2.3\text{x}10^{2}$
Ref. [32]	Dual comb	$1\text{x}10^{-3}$	$6.1\text{x}10^{-4}$	3	$4.9\text{x}10^{3}$
Ref. [33]	FTIR	$1.9\text{x}10^{-5}$	$1.2\text{x}10^{-5}$	4.7	$4.0\text{x}10^{5}$
Ref. [33]	EC-QCL	$4.4\text{x}10^{-5}$	$2.7\text{x}10^{-5}$	4.4	$1.6\text{x}10^{5}$

Extended Data Table 1.

Dynamic range comparison for state-of-the-art broadband vibrational spectroscopies. FRS: field resolved spectroscopy, ASOPS: asynchronous optical sampling. Dual comb: dual comb spectroscopy, FTIR: Fourier-transform infrared spectroscopy, EC-QCL: external-cavity quantum-cascade laser. The minimal absorbance A_{min} is determined in an equivalent manner to the first paragraph of the supplementary text, assuming a noise proportional to the intensity, $A_{\text{min}} = \frac{\sqrt{2}}{\log(10)}\delta I$ where δI is the relative standard deviation of intensity or RMS (root-mean-square) noise. The maximum absorbance A_{max} is estimated with the sample transmitted intensity being equal to the noise of the reference intensity: $A_{\text{max}} = -\log_{10}(\delta I)$. In Ref.[33] the RMS value of the absorbance is given and thus used as the basis for the calculations.

	T_{int} [ms]	SNR for T_{int}	SNR for $T_{\text{int}} = 1$ s	P_{avg} [mW]	f_{rep} [MHz]	ν_c [THz]	τ_p [fs]	w [µm]	**$E_{\min}$ [mV/cm]**	**η_{total} [%]**
Ref.[12]	2.4 [i]	$1.4\text{x}10^6$ [ii]	$2.9\text{x}10^7$	12 [ii]	28	34.2	60	35	**26**	**0.5**
Here	1000	$1.6\text{x}10^8$	$1.6\text{x}10^8$	12	50	33	100	35	**2.2**	**7.5**

Extended Data Table 2.

State-of-the-art EOS detection efficiency and sensitivity (i.e., minimum measurable field strengths). [i] Lock-in time constant of 183 µs (internal knowledge) with a 6th order filter; the settling time to reach 99 % signal strength was assumed to be the integration time (T_{int}), calculated according to the Zurich Instruments manual. [ii] Calculated from Ref.[12] for the 500-µm-thick GaSe crystal, and a chopped average power of 12 mW (internal knowledge). From the attenuation experiment (Extended Data Fig. 2), the intensity noise floor of a single measurement corresponds to 5×10^{-13}, related to the maximum spectral intensity (in the frequency domain). τ_p: (estimated) FWHM pulse durations, w: $1/\text{e}^2$ gate pulse beam radius. The minimum measurable field strength is determined for SNR=1 for an integration time per temporal element of 1 s. Scaling of the SNR with the square-root of the integration time is assumed. In order to include the effect of chopping, the average power was doubled for the field-strength calculation:

$$E\left[\frac{\text{mV}}{\text{cm}}\right] = \sqrt{\frac{4\times P_{\text{avg}}\,[\text{W}]}{SNR_{1s}\times f_{\text{rep}}[\text{Hz}]\times\tau_p[\text{s}]\times w^2[\text{cm}^2]\times\pi\times c\left[\frac{\text{m}}{\text{s}}\right]\times\epsilon_0\left[\frac{\text{As}}{\text{Vm}}\right]}}.$$

thickness GaSe [μm]	$\eta_{\text{conversion}}$ [%]	$\eta_{\text{interaction}}$ [%]	η_{BPF} [%]	η_{Fresnel} [%]	spectrally averaged η_{total} [%]	peak of $\eta_{\text{total}}(\omega)$ [%]	spectral range with >1% of $\eta_{\text{total}}(\omega)$ [cm^{-1}]	E_{min} [mV/cm]
308	10	60	25	87	3.7	7.4	600-1300	3.6
541	22	70	27	87	7.5	16.6	900-1270	2.2

Extended Data Table 3.

Comparison of the various efficiency values for two different thicknesses of GaSe crystals used as the nonlinear medium in the EOS detection.

Lit.	Method	Spectral coverage [cm^{-1}]	Cell length [m]	Resolution [cm^{-1}]	Species	Acq. time [s]	LOD [ppb]	Min. column density [molecules/cm^2 Hz$^{-1/2}$]	Noise equivalent absorbance [AU Hz$^{-1/2}$]	Corrected noise equivalent absorbance [AU Hz$^{-1/2}$]
Here	FRS	666-1430	0.45	3.1	CH_3OH C_2H_2 CH_4	80	0.8 0.6 40	8.6×10^{12} 6.3×10^{12} 4.3×10^{14}	2.9×10^{-6} 1.3×10^{-5} 5.8×10^{-5}	8.8×10^{-5} 4.1×10^{-4} 1.8×10^{-3}
Ref. 13	FRS ASOPS	500-2000	0.15	3.3×10^{-3}	CO_2	1320	1×10^{4}	5.8×10^{14}	1	1
Ref. 32	Dual comb	1820-3250	76	3.8×10^{-3}	CO_2 OCS	720	2 7	3.3×10^{13} 1.1×10^{14}	2.7×10^{-2} 2.7×10^{-2}	2.9×10^{-2} 2.9×10^{-2}
Ref. 42	Dual comb	830-2500	0.15	3.3×10^{-3}	CH_3OH	100	1×10^{6}	1.7×10^{16}	7.0×10^{-2}	7.2×10^{-2}
Ref. 43	WMS with EC-QCL	920-1150	2.64	0.1	CH_3OH C_2H_4	10	20 25	4.5×10^{14} 5.6×10^{14}	2×10^{-4} 3×10^{-4}	1×10^{-3} 1.7×10^{-3}

Extended Data Table 4.

Comparison of state-of-the-art broadband infrared spectroscopy experiments. FRS: field resolved spectroscopy, ASOPS: asynchronous optical sampling. Dual comb: dual comb spectroscopy, WMS: wavelength modulation spectroscopy, EC-QCL: external-cavity quantum-cascade laser. The limit of detection indicates the sensitivity of the instrument for a given molecular species. The minimum column density per second allows for the comparison under consideration of interaction length and integration time. In order to quantify the instrument performance independent of the environment (pressure, temperature) and absorption cross section, the noise-equivalent absorbance is given in the table. The last column indicates the noise-equivalent absorbance adjusted to a resolution of 3.3×10^{-3} cm^{-1} considering the necessary increase in integration time and assuming statistical averaging. The red values are determined from simulations using HAPI.